Supplementary Material for "Observation of Breathing Dark Pulses in Normal Dispersion Optical Microresonators"

Chengying Bao[1,‡,*], Yi Xuan[1,2], Cong Wang[1], Attila Fülöp[3], Daniel E. Leaird[1], Victor Torres-Company[3], Minghao Qi[1,2], and Andrew M. Weiner[1,2†]
[1] *School of Electrical and Computer Engineering, Purdue University, 465 Northwestern Avenue, West Lafayette, Indiana 47907-2035, USA*
[2] *Birck Nanotechnology Center, Purdue University, 1205 West State Street, West Lafayette, Indiana 47907, USA*
[3] *Photonics Laboratory, Department of Microtechnology and Nanoscience, Chalmers University of Technology, SE-412 96 Gothenburg, Sweden and*
[‡] *Present address: T. J. Watson Laboratory of Applied Physics, California Institute of Technology, Pasadena 91125, USA*

1. Experimental methods

Line-by-line pulse shaping. The pulse shaper is used for time domain characterization. The method for shaping the output comb into transform-limited pulses is described in ref. [S1]. Comb lines with mode number in the range $[-7,\ 11]$ (relative to the pump) are used for pulse shaping. The intensity of the comb lines is adjusted to prevent the strongest comb lines from dominating the pulse shaping. In this intensity adjustment, the pump line (mode 0) is attenuated by 20 dB; modes ±1 are attenuated by 10 dB; modes ±2 are attenuated by 5 dB, and the other modes are not attenuated. The autocorrelation (AC) is measured by a noncollinear second-harmonic generation based intensity autocorrelator.

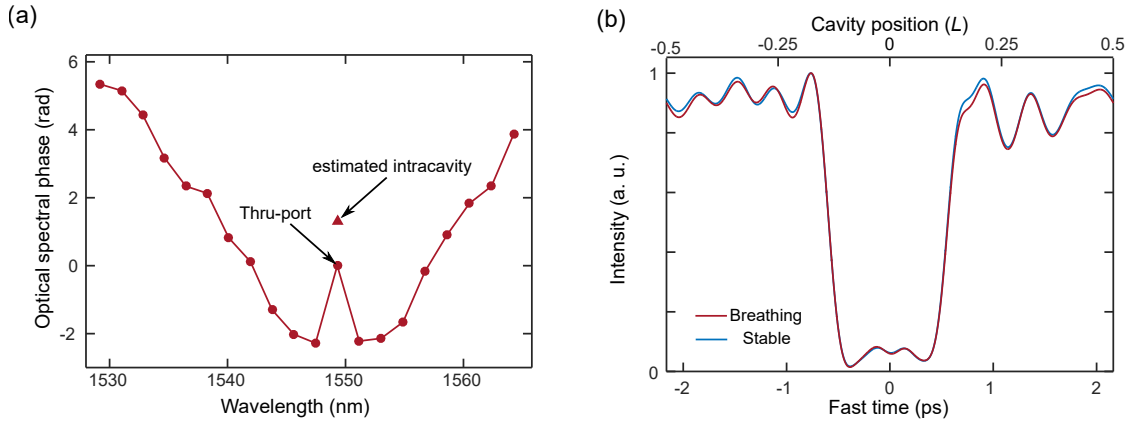

FIG. S1: **Intracavity waveform retrieval.** (a) The retrieved comb phase via line-by-line pulse shaping. The intracavity pump phase is estimated based on the through-port data. (b) Using the averaged power spectra of the stable dark pulse and the breathing dark pulse together with the retrieved phase, the intracavity waveform can be reconstructed, showing a dark-localized waveform. Note that points on the fast time axis are equivalent to spatial positions within the cavity (L is the cavity round trip length).

Intracavity waveform retrieval. Using the comb phase retrieved in line-by-line pulse shaping (the mode-locked state and the breathing state share a nearly identical phase profile as shown in Fig. 3(a) of the main text), the intracavity waveform for the device characterized in the main text can be reconstructed [S2]. Note that the pump line in the through-port contains both the transmitted uncoupled pump and the coupled-out component from the cavity. Hence, the intensity and phase in the through-port are corrected to yield the pump line in the cavity, based on the method described in ref. [S2] and the Supplementary Information therein. By applying the retrieved phase in

*Electronic address: cbao@caltech.edu
†Electronic address: amw@purdue.edu

Fig. S1(a) to the spectra of the breathing dark pulse and the stable dark pulse, we obtain dark-localized waveforms (Fig. S1(b)). Since the breathing dark pulse breathes weakly, this confirms that the breathing dark pulse retains a dark-localized waveform.

Fast comb breathing recording. The method to record the fast evolution of the spectral breathing is the same as that used in ref. [S3]. A pulse shaper is used to select individual comb lines, and the output is recorded by a fast photodetector and amplified by a low noise amplifier. A portion of the output prior to the pulse shaper is used to trigger the oscilloscope in order to provide a timing reference for measurements performed on different comb lines. The recorded traces are Fourier transformed and numerically filtered by a 20 MHz bandpass filter to isolate the strongest breathing tone; the filtered spectra are inverse Fourier transformed to yield the spectral breathing traces analyzed in Fig. 3.

2. Numerical simulations details

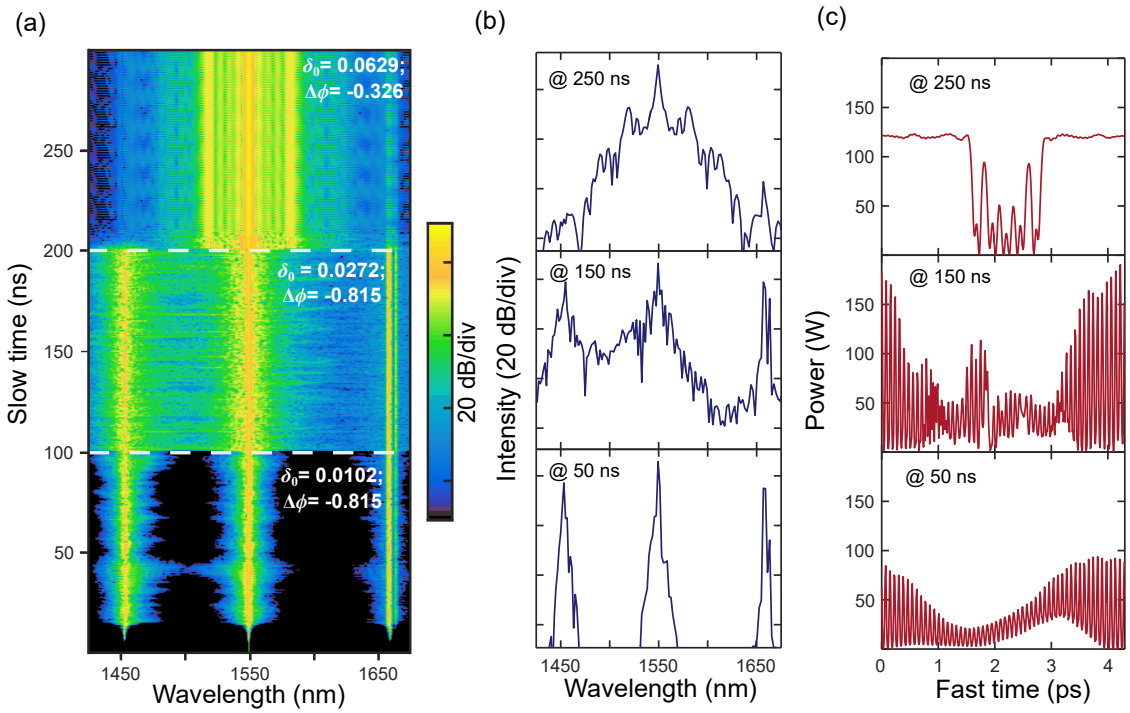

FIG. S2: **Tuning the detuning to generate the breathing dark pulse.** (a) The spectral dynamics while the detuning and mode interaction parameter $\Delta\phi$ are varied. (b) Typical spectra at 50 ns, 150 ns and 250 ns; at 250 ns, spectrum with characteristic dark pulse Kerr comb is obtained. (c) Typical waveforms at 50 ns, 150 ns and 250 ns; the waveform at 250 ns confirms that the breathing state retains the dark-localized waveform.

Simulated comb generation dynamics. To initiate the comb generation from noise, mode interaction is included in simulations. To include mode interaction, we add an identical phase shift $\Delta\phi$ per round trip to 4 modes within the range $[-57, -54]$ relative to the pump. In Fig. S2(a), we show the simulated breathing dark pulse generation dynamics. During the first 100 ns, we set δ_0=0.0102 (frequency detuning 377.5 MHz), $\Delta\phi$ =−0.815; the comb is initiated by the mode interaction and coarsely spaced. During the second 100 ns, we set δ_0=0.0272 (frequency detuning 1006.7 MHz), $\Delta\phi$ =−0.815; the comb grows and becomes chaotic. During the third 100 ns, δ_0=0.0629 (frequency detuning 2328.1 MHz), $\Delta\phi$ =−0.326, a breathing dark pulse can be obtained. The change in the mode interaction strength in this step can be attributed to thermal effects and change of intracavity power when tuning the laser further into resonance [S2]. Since the full evolution over 200−300 ns are plotted in Fig. S2(a), it is hard to resolve the breathing dynamics. For visualization of the breathing on a smaller time scale, see Fig. 1 in the main text. In Figs. S2(b, c), we show the typical spectra and waveforms (at 50 ns, 150 ns, 250 ns) in each step. Note that the chaotic comb during the period 100−200 ns (prior to breathing dark pulse formation) is distinct from the chaotic breathing in Fig. 4 of the main text, and the time-domain waveform and spectrum do not resemble those in the stable dark pulse state.

Numerical pulse shaping and AC in Figs. 3, 4. For the AC traces presented in Fig. 3(b) and Fig. 4(d) of the main text, we extract the simulated phase of the stable dark pulse, which we denote as $\phi_{\rm dp}(\omega)$, and then add $-\phi_{\rm dp}(\omega)$ to compensate the phase and obtain a transform-limited pulse. The AC is then calculated. For the periodic breathing and chaotic breathing comb, the same $-\phi_{\rm dp}(\omega)$ is added to the complex spectral amplitude. Then a series of AC traces are computed based on snapshots of the intensity profile. 10^4 individual AC traces are calculated in a 1 μs time window (equivalent to $\sim$782 periods for the regular breathing dark pulse) and averaged to yield the traces in Fig. 3(b) and Fig. 4(d). All the simulated comb modes are used in the simulated pulse shaping; hence, the width of the AC trace is shorter than the experiments, where only a subset of the lines are accommodated by our pulse shaper. The intensity of the comb lines within $[-2,\ 2]$ (relative to the pump) are adjusted in the same way used in the line-by-line pulse shaping in experiments.

3. Breathing dark pulses characterized by an optical sampling oscilloscope

Breathing dark pulses generated in 'Device 2' are characterized by an optical sampling oscilloscope. This microresonator also has a free-spectral-range of 231 GHz and the loaded Q-factor is $\sim$1 million. The breathing dark pulse is generated when we increase the pump power slightly after generating the mode-locked dark pulse. In contrast to 'Device 1' discussed in the main text, the optical and RF spectra are measured from the drop-port (shown in Figs. S3(b, c)), which provides a direct replica of the intracavity field without the complication of a strong superimposed pump field [S4]. The breathing frequency is 635 MHz, which as before is well outside the half-width-half-magnitude (HWHM) of the cavity resonance. This breathing frequency is slightly lower than that reported breathing rate in the main text, which can be attributed to the slightly higher loaded-Q factor and smaller resonance linewidth. The breathing dark pulses are measured in the time domain by an equivalent-time optical sampling oscilloscope (OSO) with 500 GHz bandwidth. The OSO is based on four-wave-mixing optical sampling in a nonlinear fiber [S5]. The sampling gate is provided by a mode-locked laser whose repetition rate is asynchronous to the input signal. Hence, the delay between the pulse under test and the sampling gate is automatically swept. In Fig. S3(d), the waveform is reconstructed by using the breathing dark pulses as trigger, which further supports the observation that the breathing dark pulse retains a dark-localized waveform. Since the breathing frequeny and the repetition rate of the breathing dark pulses Kerr comb are incommensurate, it is not possible to resolve the breathing dynamics within a full breathing period with an equivalent-time sampling oscilloscope. However, the OSO can be triggered instead by the 635 MHz breather frequency, as indicated in the schematics in Fig. S3(a). In this case, the variation of the power levels within the dark pulses over the breathing period can be clearly observed but their structure is washed out (see Fig. S3(e)). We further analyzed the occurrence probability for different power levels for the OSO measurement. The histogram in Fig. S3(f) (analyzed from the measurement in Fig. S3(d)) shows two peaks, which reflects the low-power-level (waveform hole) and high-power-level (waveform background) of the breathing dark pulse. When further analyzing the power-level occurrence probability within different time slots using the measurement shown in Fig. S3(e), we can clearly observe the change of the most probable low-power-level and high-power-level. This shows the dark-localized waveform is varying in the time domain. Furthermore, the change in the probability of the low-power-level peak and high-power-level peak suggests slight changes in the duty cycle of the dark pulse.

4. Breathing dark pulses in the absence of mode interaction

The mode interaction is an important perturbation to Kerr comb generation in microresonators. It has recently been found that mode interaction can induce breathing of bright solitons in anomalous dispersion microresonators [S6]. Here, we show that mode interaction is not required for the breathing of the dark pulse studied in our device. In experiments, we first generate the breathing dark pulse at a relatively low chip temperature, similar to experiments in Figs. 1, 2 of the main text. Then, we increase the chip temperature which shifts the resonance (the pump wavelength is tuned accordingly to follow the shifted resonance), while maintaining the breathing comb. At a relatively high temperature, the spectral spike around 1657 nm vanishes (Fig. S4(a)), indicating the mode interaction is relatively weak. The change in the strength of the mode interaction may be understood as arising from different temperature dependent frequency shifts for resonances corresponding to different spatial modes. The comb is observed to retain the breathing (Fig. S4(b)). With the same parameters as used in Fig. 1 of the main text, numerical simulations still show the breathing of the dark pulse (see Figs. S4(c, d)) when turning off the mode interaction term (i.e., setting $\Delta\phi$=0). Furthermore, the simulated spectrum (averaged over slow time t) when turning off the mode interaction term also closely matches the experiments. These experimental and numerical results show that the breathing of dark pulse observed here is not caused by the mode interaction.

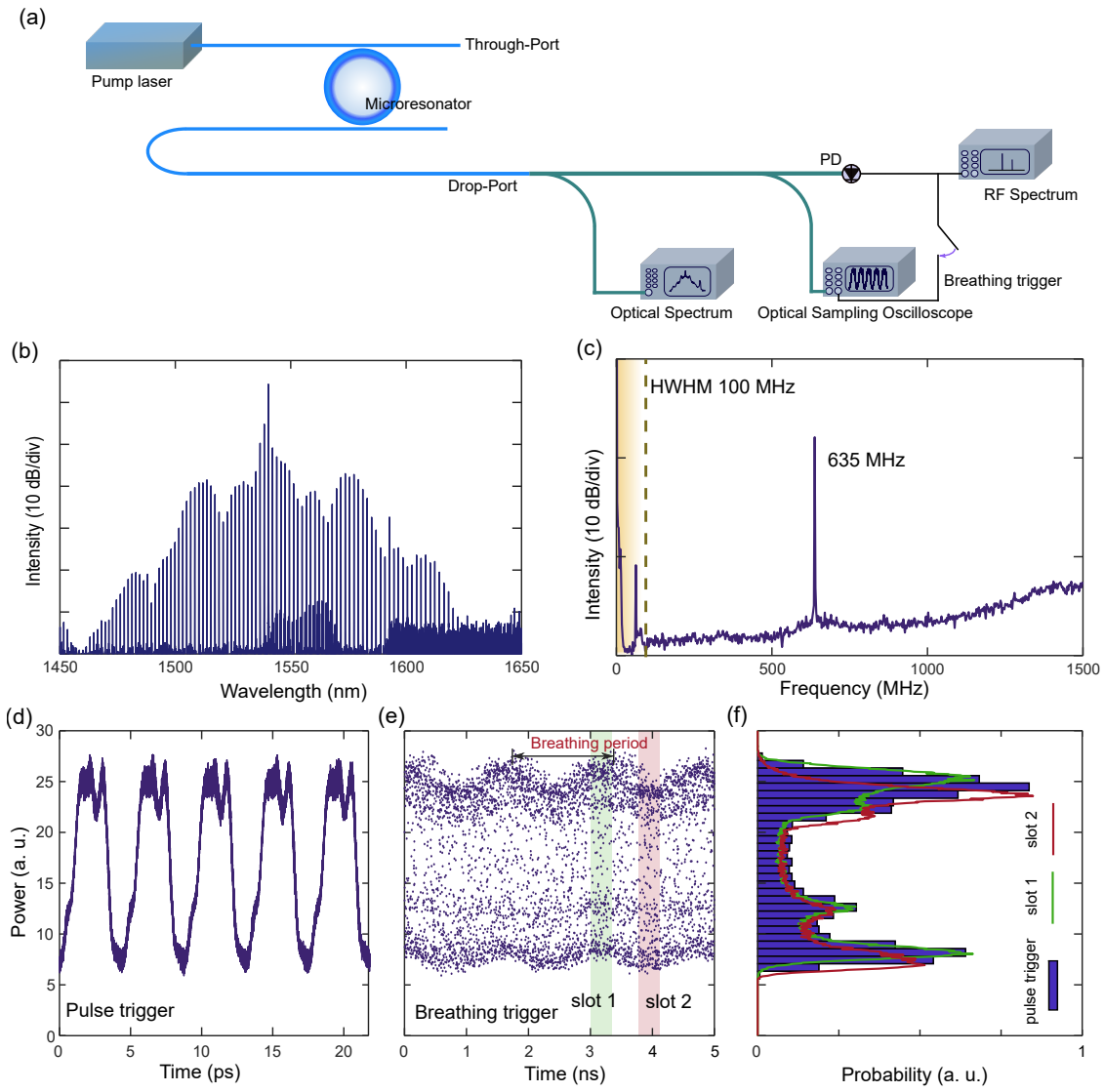

FIG. S3: **Characterization of breathing dark pulses by an optical sampling oscilloscope.** (a) Experimental setup of the generation and characterization of breathing pulses in another chip (Device 2). A commercially available equivalent-time optical sampling oscilloscope (OSO) is used for the time domain characterization. A breathing dark pulse is obtained when increasing the pump power slightly from the stable dark pulse state. The optical spectrum and the RF spectrum are shown in (b) and (c) respectively. Note that the measurements are performed at the drop-port as it allows direct characterization of the intracavity field without the superimposed pump. (d) Intracavity waveform of the breathing state as measured by the OSO when it is triggered by the optical pulses themselves; a dark-localized waveform is observed. (e) When the OSO is instead triggered by the 635 MHz breathing frequency, the equivalent-time nature of the oscilloscope washes out the individual pulses, as the breathing period does not correspond to an integer multiple of the pulse round trip time. (f) Occurrence probability for different certain power-levels. The histogram is analyzed from the measurement triggered by the input pulses shown in (d), while green and red lines are analyzed from measurement within different time slots (corresponds to the shaded regions in (e)) when the OSO is triggered by the breathing frequency.

5. Illustration of animations

Animation 1, spectral and temporal breathing of the periodic breathing dark pulse (corresponds to Fig. 1 in the main text). The breather repeats itself around 1.2∼1.3 ns and ∼2.5 ns (end of the animation), as the period is 1.27 ns.

Animation 2, spectral and temporal breathing of the chaotic breathing dark pulse (corresponds to Fig. 4 in the

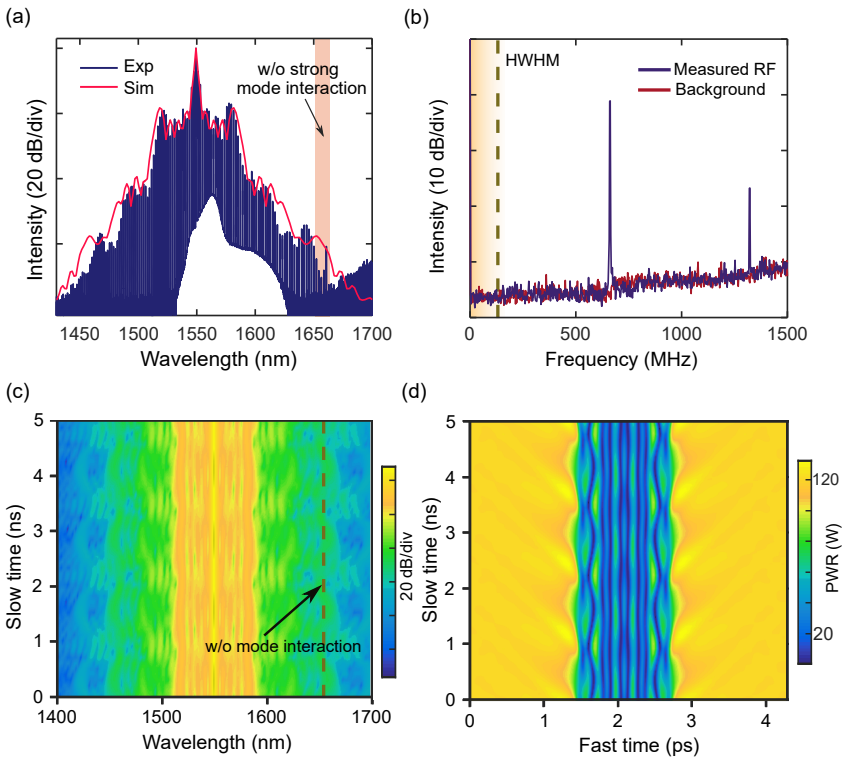

FIG. S4: **Experimentally observed (a, b) and simulated (c, d) breathing dark pulses in the absence of strong mode interaction.** (a) By changing the chip temperature, the mode interaction strength can be reduced such that there is no significant spike in the spectrum around 1657 nm. The simulated (averaged over slow time) spectrum when turning off the mode interaction term closely matches the experimentally measured spectrum. (b) Breathing is also observed without the strong mode interaction. (c) Spectral breathing is also observed in simulations in the absence of the strong mode interaction, using the other parameters which are the same as in Fig. 3 of the main text. (d) The corresponding temporal breathing.

main text). The chaotic breather does not repeat itself in the full 2.5 ns.

[S1] F. Ferdous, H. Miao, D. E. Leaird, K. Srinivasan, J. Wang, L. Chen, L. T. Varghese, and A. M. Weiner, Nature Photonics **5**, 770 (2011).
[S2] X. Xue, Y. Xuan, Y. Liu, P.-H. Wang, S. Chen, J. Wang, D. E. Leaird, M. Qi, and A. M. Weiner, Nature Photonics **9**, 594 (2015).
[S3] C. Bao, J. A. Jaramillo-Villegas, Y. Xuan, D. E. Leaird, M. Qi, and A. M. Weiner, Phys. Rev. Lett. **117**, 163901 (2016).
[S4] P.-H. Wang, Y. Xuan, L. Fan, L. T. Varghese, J. Wang, Y. Liu, X. Xue, D. E. Leaird, M. Qi, and A. M. Weiner, Opt. Express **21**, 22441 (2013).
[S5] P. A. Andrekson and M. Westlund, Laser & Photonics Reviews **1**, 231 (2007).
[S6] H. Guo, E. Lucas, M. H. Pfeiffer, M. Karpov, M. Anderson, J. Liu, M. Geiselmann, J. D. Jost, and T. J. Kippenberg, Phys. Rev. X **7**, 041055 (2017).